As-Run Thermal Analysis of the GTL-1 Experiment Irradiated in the ATR South Flux Trap
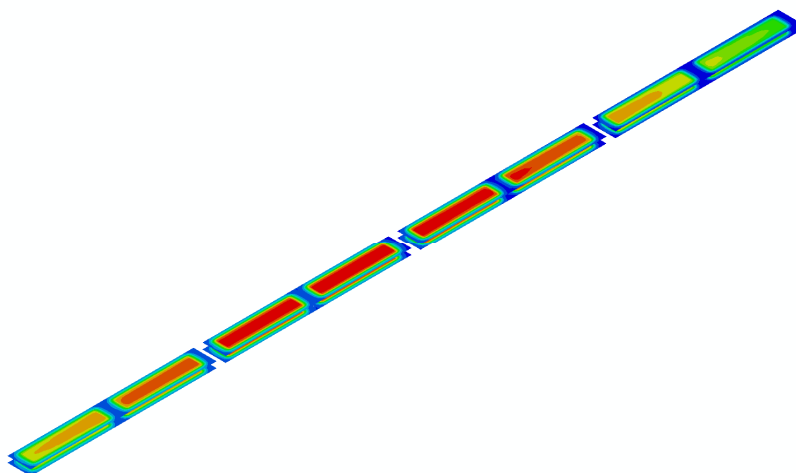
Donna P. Guillen

May 2011

INL
Idaho National
Laboratory

As-Run Thermal Analysis of the GTL-1 Experiment Irradiated in the ATR South Flux Trap

Donna P. Guillen

May 2011

Idaho National Laboratory
Next Generation Nuclear Plant Project
Idaho Falls, Idaho 83415

As-Run Thermal Analysis of the GTL-1 Experiment Irradiated in the ATR South Flux Trap

INL/EXT-11-21975

May 2011

Prepared by:
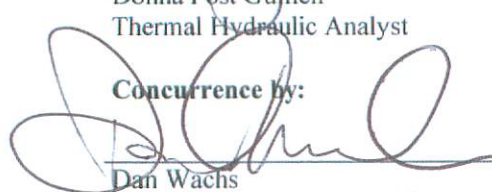
_____   _____
Donna Post Guillen   5/12/11
Thermal Hydraulic Analyst   Date

Concurrence by:
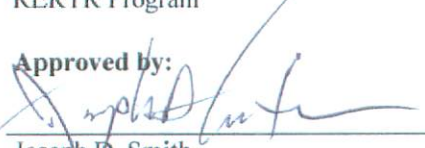
_____   _____
Dan Wachs   5/15/11
RERTR Program   Date
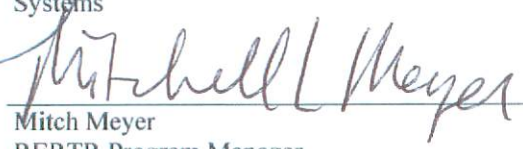
Approved by:

_____   _____
Joseph D. Smith   12 May 2011
Department Manager, Advanced Process and Decision   Date
Systems

_____   _____
Mitch Meyer   5/17/11
RERTR Program Manager   Date

ABSTRACT

The GTL-1 experiment was conducted to assess corrosion performance of the proposed Boosted Fast Flux Loop booster fuel at heat flux levels ~30% above the design operating condition. Sixteen miniplates fabricated from 25% enriched, high-density (4.8 g-U/cm^3) U_3Si_2/Al dispersion fuel with 6061 aluminum cladding were subjected to peak beginning of cycle (BOC) heat fluxes ranging from 411 W/cm^2 to 593 W/cm^2. Miniplates fabricated with three different fuel variations (without fines, annealed, and with standard powder) exhibited negligible irradiation-induced swelling and a normal fission density gradient. Both the standard and the modified prefilm procedures produced hydroxide films that adequately protected the miniplates from excessive surface corrosion.

A detailed finite element model was constructed to calculate temperatures and heat flux for an as-run cycle average effective ATR south lobe power of 25.4 MW(t). Results of the thermal analysis are given at four times during the cycle: BOC at 0 effective full power days (EFPD), middle of cycle (MOC) at 18 EFPD, MOC at 36 EFPD, and end of cycle at 48.9 EFPD. The highest temperatures and heat fluxes occur at the BOC and decrease in a linear manner throughout the cycle.

Miniplate heat flux levels and fuel, cladding, hydroxide, and coolant-hydroxide interface temperatures were calculated using the average hydroxide thickness on each miniplate measured during post-irradiation examination. The hydroxide layers are the largest on miniplates nearest to the core midplane, where heat flux and temperature are highest. The hydroxide layer thickness averages 20.4 μm on the six hottest miniplates (B3, B4, C1, C2, C3, and C4). This tends to exacerbate the heating of these miniplates, since a thicker hydroxide layer reduces the heat transfer from the fuel to the coolant. The computational results indicate that fuel centerline temperature increases by approximately 2.25°C per μm of hydroxide thickness. Assuming EOC hydroxide layer thickness, these six hottest miniplates have the following thermal characteristics at BOC:

- Peak fuel centerline temperature >300°C

- Peak cladding temperature >200°C

- Peak hydroxide temperature >190°C

- Peak hydroxide-water interface temperature >140°C

- Peak heat flux >565 W/cm^2.

CONTENTS

FIGURES

TABLES

ACRONYMS

ATR	Advanced Test Reactor
BFFL	Boosted Fast Flux Loop
BOC	beginning of cycle
ECAR	Engineering Calculations and Analysis Report
EDF	Engineering Design File
EFPD	effective full power days
EOC	end of cycle
GTL	Gas Test Loop
INL	Idaho National Laboratory
IPT	inpile tube
MOC	middle of cycle
PIE	post-irradiation examination
RERTR	Reduced Enrichment for Research and Test Reactors
SFT	south flux trap

As-Run Thermal Analysis of the GTL-1 Experiment Irradiated in the ATR South Flux Trap

1. INTRODUCTION

Gas Test Loop (GTL) irradiation experiment GTL-1 was sponsored by the U.S. Department of Energy as part of the GTL project (which later became the Boosted Fast Flux Loop [BFFL] project) to determine the feasibility of designing, constructing, and installing an experimental vehicle in an existing host irradiation facility that can replicate, with reasonable fidelity, the fast-flux test environment needed for irradiation testing of new fuels and materials. The technical and functional requirements for the BFFL stipulate a minimum neutron flux intensity (10^{15} n/cm^2·s) and fast-to-thermal neutron ratio (>15) for the test environment (Longhurst and Khericha 2005). To achieve the necessary neutron flux levels, a system comprised of booster fuel and thermal neutron filters was designed for incorporation in the northwest test lobe of the Advanced Test Reactor (ATR) at Idaho National Laboratory (INL).

The desired neutron flux characteristics led to the selection of high-density (4.8 g-U/cm^3) U$_3$Si$_2$/Al dispersion fuel plates clad with 6061 aluminum for the BFFL booster fuel. Uranium silicide dispersion fuel is an ideal choice for the booster fuel because it exhibits low parasitic neutron absorption and good irradiation and chemical stability (Bourns 1968). The U.S. Nuclear Regulatory Commission formally approved (NUREG-1313 1988) the use of U$_3$Si$_2$/Al dispersion fuel with uranium densities up to 4.8 g/cm^3 in domestic research and test reactors, but the new booster fuel requires demonstration because the fuel meat for the BFFL application is thicker, the radius of curvature is smaller, and the heat fluxes are higher than previous experience. In addition, experiments conducted in the Belgian Reactor 2 (BR2) reactor operated by the Belgian Nuclear Research Centre (SCK•CEN) in Mol, Belgium exhibited failure of aluminum clad U$_3$Si$_2$/Al dispersion fuel plates loaded to 6.0 g-U/cm^3 and exposed to heat fluxes on the order of 5.5 MW/m^2 (Leenaers et al. 2004). In that instance, fuel plate failure was attributed to inadequate cooling that led to the accelerated corrosion of the AG3-NET Al–Mg alloy (nuclear grade Al-5754) cladding. Once highly corroded, the "much lower thermal conductivity of the corrosion layer (2.25 W/m-K) compared to AG3-NET alloy (130 W/m-K)" caused an "increase in temperature of the cladding." The "calculations show that the cladding reached temperatures in excess of 300°C" and "at these high temperatures, progressing sensitization of the aluminum-magnesium cladding leads to the decoration of the grain boundaries with Mg$_2$Al$_3$ precipitates, making the cladding susceptible to grain boundary corrosion" (Leenaers et al. 2004).

To avoid potential runaway corrosion of the ATR driver fuel, prior to reactor operation the fuel plates are autoclaved with a water solution at a controlled temperature, pressure, and pH to form a stable, protective hydroxide layer (a crystalline, nonporous gamma-alumina hydrate or boehmite). Application of a very thin boehmite layer serves to passivate the cladding surface, which inhibits corrosion product buildup during irradiation and subsequent hydroxide spalling (Shaber and Hofman 2005). Prefilming the fuel cladding is an important protective measure because hydroxide layers formed in the presence of neutron radiation tend to grow much thicker, are more subject to erosion, and are less resistant to chemical attack (Byalobzheskii 1962).

There are several key differences between the BR2 plate failure and the BFFL booster fuel design. The BR2 fuel plates were not pretreated, used a cladding alloy with a different composition, and experienced different coolant chemistry and flow. The BFFL fuel plates are designed with Al-6061 cladding, which has different composition and physical properties than the AG3-NET cladding. Lack of data on prefilmed fuel plates similar in composition to the proposed BFFL booster fuel and operating under similar conditions prompted inpile tests to be conducted for representative samples of the proposed BFFL booster fuel.

Irradiation testing of miniplates with prototypic construction was conducted at heat fluxes and coolant flow velocities typical of the booster fuel. Miniplates were exposed to peak heat fluxes up to 593 W/m^2 (2.622 Btu/s·in^2), which bounds the nominal BFFL booster fuel operating heat flux levels of 450 W/m^2 (2.75 Btu/s·in^2). The primary objectives of the experiment with respect to corrosion performance were to ensure that: (1) uncontrolled or unexpected hydroxide growth or change does not occur during irradiation, and (2) the corrosion/erosion processes do not compromise the structural properties and containment capabilities of the fuel cladding. Of interest to the BFFL program are the processes or conditions that contribute to keeping the hydroxide film thin, thus improving fuel performance.

This report documents as-run thermal evaluations for an inpile experiment (designated GTL-1) conducted at high heat flux for the purpose of assessing the performance of 25% enriched, high-density (4.8 g-U/cm^3) U$_3$Si$_2$/Al dispersion fuel miniplates clad with 6061 aluminum and pretreated with a stable hydroxide film. The thermal analyses performed prior to irradiation were executed for a bounding case to satisfy ATR Nuclear Safety requirements (Guillen 2008). However, to draw meaningful conclusions from the GTL-1 miniplate irradiation experiment regarding the performance of the hydroxide film on the miniplates, it is necessary to perform a thermal analysis at the actual power levels experienced during irradiation. A Monte Carlo Neutron Particle physics analysis provided as-run fuel fission heat generation rates at four times during ATR Cycle 143A for the GTL-1 fuel miniplates irradiated in the ATR south flux trap (SFT) irradiation test position as shown in Figure 1 (Perez and Chang 2010). Post-irradiation examination (PIE) measurements of hydroxide layer thickness on each of the 16 fueled miniplates (Robinson 2008) were also used in the thermal analysis. Heat flux and temperatures for the miniplate fuel, cladding, hydroxide, and coolant-hydroxide interface are presented at beginning of cycle (BOC) at 0 effective full power days (EFPD), middle of cycle (MOC) at 18 EFPD, MOC at 36 EFPD, and end of cycle (EOC) at 48.9 EFPD.

These evaluations were requested by Reduced Enrichment for Research and Test Reactors (RERTR) project staff. Recommendations for future work are provided. Such studies are necessary to gain a better understanding of the hydroxide layer formed during irradiation.
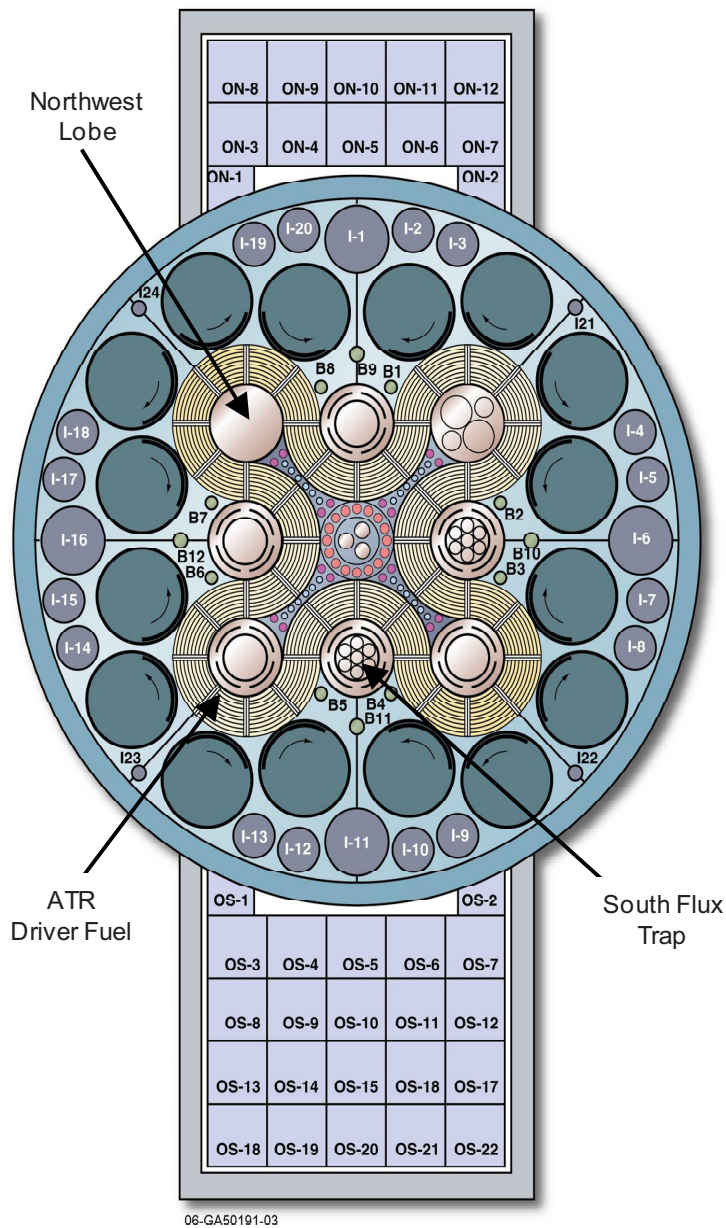
Figure 1. Illustration of the ATR core arrangement and irradiation positions.
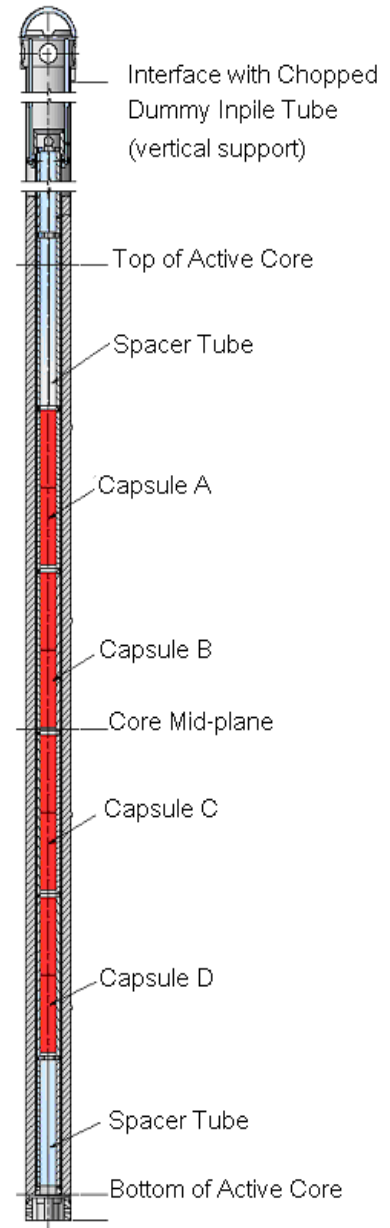
Figure 2. GTL-1 irradiation test assembly.

3

2. EXPERIMENT DESCRIPTION

2.1 Experiment Design

The GTL-1 irradiation experiment contains 16 miniplates housed in four interconnecting flow-through capsules, designated as A, B, C, and D, with A at the top of the test assembly and D at the bottom as shown in Figure 2. There are four miniplates in each capsule arranged vertically in a 2 × 2 array (each capsule has two axial levels, with two miniplate positions per level). Within each capsule, the miniplate positions are designated as 1 and 2 in the upper level and 3 and 4 in the lower level. Figure 3 shows the arrangement of the miniplates within the four capsules. The test matrix consisted of three different fuel fabrication variations: two miniplates without fines, one miniplate with annealed powder, and 13 with standard powder. All miniplates received a prefilming treatment. The faces of the miniplates were oriented "edge-on," such that they were parallel to a radial line from the core center through the center of the SFT position as shown in Figure 4. The miniplates are 2.5 cm wide and 10.2 cm long. The fuel meat thickness of all plates is 0.102 cm, the cladding is 0.076 cm on either side of the fuel, and the total plate thickness is 0.254 cm. These plates are referred to as "double-thick" since the fuel meat thickness is twice that of a standard materials test reactor type fuel plate. The increased thickness is necessary to produce the high heat flux levels. A 6061 aluminum border surrounds the 9.5 × 1.83 cm fuel region. Inside of each capsule, the two columns of two miniplates are arranged end-to-end, with no spacing between the plates in the flow direction (the bottom end of the upper plate rests against the top end of the lower plate), measuring 20.3 cm long. There is a 0.98 cm axial separation between fuel plates in adjacent capsules (Hayes 2008).

Figure 3. GTL-1 miniplate arrangement.
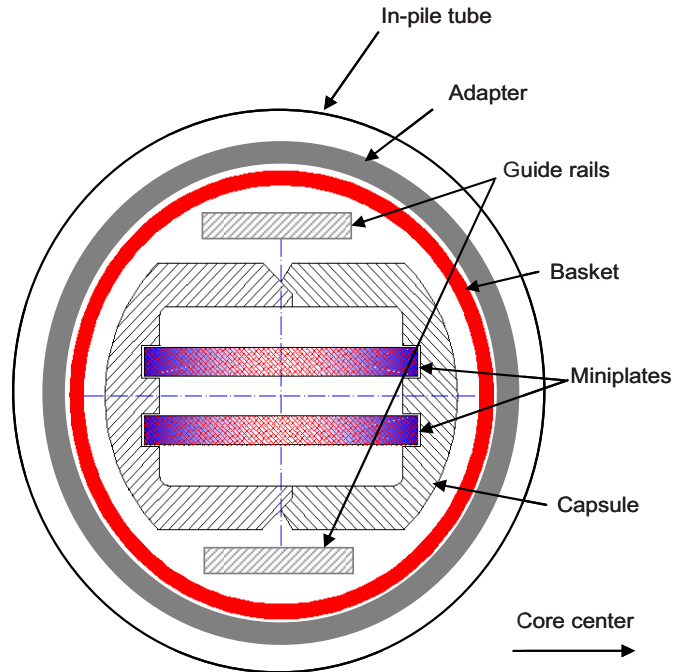
Figure 4. Cross-section of GTL-1 experiment assembly.

4

The miniplates were prefilmed in an autoclave prior to irradiation to produce a uniform, adherent boehmite ($Al_2O_3 \cdot H_2O$) layer on the cladding surface. The treatment was performed in an autoclave vessel filled with pH adjusted water. The recipe for the prefilm treatment calls for autoclaving with deionized water at a temperature of $185 \pm 8°C$ and a pressure of 0.896 ± 0.207 MPa held for 18 ± 1 hr starting when the 185°C temperature is reached. Prior to the treatment, the plates were chemically cleaned with a heated sodium hydroxide bath and a nitric acid etch to remove surface oxides. Thirteen of the 16 miniplates were pretreated with a surface boehmite layer (nominally 2.0 μm thick) formed in an autoclave using deionized water with a pH of 7.8. This is referred to as the "standard" prefilm treatment. The remaining three miniplates (A2, C2, and D4) were pretreated with a thinner boehmite layer (nominally 0.5 μm thick) deposited using a similar procedure with water at a pH of 5.7. This is referred to as the "modified" prefilm treatment (Hayes 2008). The prefilm thickness was measured using SEM photos of smooth surfaces located between regions where hydroxide had formed around surface connected precipitate particles. Although the modified prefilming process had not previously been tested in the ATR, it was expected that the fuel thermal performance with the thinner insulating layer of boehmite would be better than the standard prefilm. Since the water pH used to produce the modified prefilm more closely matches the pH of the ATR primary coolant, it is expected to be more stable and resistant to growth during irradiation. A hydroxide layer that remains thin during irradiation is sought to maximize heat transfer from the fuel to the coolant. The thermal conductivity of this prefilm boehmite layer is approximated as 2.25 W/m-K over the temperature range from 394 to 505 K, based on ex-reactor studies (Polkinghorne and Lacy 1991).

2.2   Power History

The miniplates in the GTL-1 experiment were irradiated in the ATR SFT position at a significant performance margin above the BFFL design condition. The BFFL booster fuel is intended to operate under relatively aggressive conditions, characterized by a thermal heat flux of 450 W/cm². The experiment was designed to expose the miniplates to heat fluxes ranging from about 400 to 600 W/cm² (2.44 to 3.67 Btu/s·in²). The higher power levels were included in the experiment to explore a margin of safety above the expected operating power level.

The power levels of the surrounding lobes affect the power in the flux trap. Based on the power history for ATR Cycle 143A, this experiment experienced an average effective south lobe source power of 25.4 MW(t) (based upon Center lobe at 24.3 MW(t), Southwest lobe at 26.9 MW(t), and Southeast lobe at 25.0 MW(t)). The reactor was brought up to full power on September 23, 2008. A scram occurred on October 16, 2008 and the reactor was restarted on November 5, 2008. Another scram occurred on November 21, 2008, caused by a problem with another experiment. The reactor was restarted on November 26, 2008, and operated through the end of the cycle, which completed on December 6, 2008. The duration of the capsule irradiation was 48.9 EFPD.

3. MODEL DESCRIPTION

3.1 Finite Element Model

The finite element model representing the physical geometry of the miniplate experiment configuration were developed and analyzed using the computer code ABAQUS Version 6.7-3 (Dassault Systèmes 2007) on the LINUX-based computing platforms dguillen and icestorm. ABAQUS CAE was used for construction of the finite element model, and ABAQUS Standard was used to calculate steady-state temperatures and heat fluxes.

The analysis was performed on a SGI Altix ICE 8200 distributed memory cluster with 512 Intel Xeon quad core 2.66 GHz processors running SUSE Linux Enterprise Server 10. The computer configurations listed in Table 1 were used to perform the calculations reported in this report.

Table 1. Computer configurations used for analysis.

Software	Version	Computer Type	Operating System	Processor	Computer Name
ABAQUS	6.7-3	SGI Altix ICE 8200 distributed memory cluster	SUSE Linux Enterprise Server 10	512 Intel Xeon quad core 2.66 GHz	icestorm
ABAQUS	6.7-3	HP xw9300 Workstation	SUSE Linux 10.2	AMD Opteron-64	dguillen #387473

A formal quality assessment for these platforms using code Version 6.7-3 has been completed for conditions applicable to this analysis and documented in the INL Engineering Calculations and Analysis Report ECAR-131 (Murray 2008). Supporting calculations were performed using MathCad Version 14.

The finite element model geometry was constructed using a combination of shells and three-dimensional solid elements (Guillen and Murray 2009). Dimensions are based upon the drawings listed in Table 2. The assembly is comprised of the miniplates, rails, capsules, spacers, basket, adapter, and coolant channels. The model includes all four capsules of the test train assembly within the active core, along with the top, upper, and bottom spacers that are used to position the capsules axially with the basket. The basket design is the same as that for the large B-position experiments. A 0.013 m thick adapter constructed of 6061 aluminum is used to fill the space between the outer diameter of the basket and the inner diameter of the chopped dummy inpile tube (IPT). The adapter was necessary because the experiment was originally designed to be inserted into a large B-position with a smaller diameter than the SFT. Primary coolant water flows through the test train, the 1.016 mm water annulus between the basket and adapter, and the 0.940 mm water annulus between the adapter and IPT. There are three water coolant channels approximately 0.36 cm thick and 2.26 cm wide in contact with the fuel plates. The main water channel through the test train includes the flow through the larger area of the top, upper, and bottom spacers, and also through the confluence regions at the end of Capsule A and beginning of Capsule B, end of Capsule B and beginning of Capsule C, and end of Capsule C and beginning of Capsule D. Small nubs on the outside diameter of the basket and adapter maintain the spacing in the adjacent water annuli. Two guide rails between the capsules and the basket serve to center the capsules radially within the basket. The total length of the portion of the assembly modeled is 1.469 m.

Table 2. GTL-1 experiment component drawing numbers and titles.

Drawing No.	Drawing Title
443027	ATR South and East Chopped Dummy IPT Assembly
600310	ATR/ATRC BFFL (GTL-1) Miniplate Adapter Assemblies
600418	ATR/ATRC BFFL (GTL-1) Miniplate SFT Adapter Back-up Assemblies
600420	ATR BFFL (GTL-1) Miniplate Inner Basket Lift Assemblies and Details
600447	ATR/ATRC BFFL (GTL-1) Miniplate Modified Large B-Position Basket Detail
600448	ATR BFFL (GTL-1) Miniplate Irradiation Assembly
600450	ATRC BFFL (GTL-1) Miniplate Irradiation Assembly
637209	GTL Experiment Assembly
630233	ATR Large B-Position Basket
630231	ATR Top Spacer Assembly
630225	ATR Upper Spacer Assembly
630229	ATR Bottom Spacer Assembly
637210	GTL Mini-Plate Capsule Assembly
637212	Capsule, GTL
637213	Capsule, Cap
637215	Fuel Plate, 0.040 Thick Fuel

3.2   Thermal Hydraulic Analysis

The ATR is cooled by pressurized (2.5 MPa) water at a pH between 4.8 and 6.0 (SAR-153 2011). During ATR Cycle 143A, the coolant pH remained above 5.01 with an average pH of approximately 5.25 (Beckwith 2011). The water chemistry specification is listed in Table 3. Coolant flow enters the experiment assembly from the top of the reactor with an inlet temperature of 52°C. Flowing water travels downward through the test train, the annulus between the basket and the adapter, and the annulus between the adapter and the IPT. Table 4 lists the flow rates in the water channels. The loss coefficients through the test train were obtained from a hydraulic flow test (Wachs 2006). Using the experimentally-derived loss coefficients, the resulting flow velocity across the miniplates is 14.6 m/s. The velocity of cooling water flowing through the annular gaps was computed from a hydraulic analysis employing the extended Bernoulli equation (Incropera and DeWitt 2002) with the inlet conditions (52°C and 2.5 MPa) and pressure drop (0.53 MPa) for two primary coolant pump operation. The calculated flow velocity is 5.1 m/s in the annular gap between the adapter and the IPT and 7.8 m/s in the annular gap between the adapter and the basket. The calculated total flow through the entire experiment assembly is 5.438×10^{-3} m^3/s. Heat transfer coefficients for turbulent forced convection to the cooling water (shown in Table 5) were obtained from the Colburn correlation using the film temperature method to account for fluid property variation (Perry and Green 1997). Thermophysical properties used for the materials comprising the miniplates are listed in the Appendix.

Table 3. Water chemistry specification (SAR-153 2011).

Parameter	Limits
Conductivity, reactor power > 3 MW	2-5 µmhos/cm
Conductivity, reactor power < 3 MW	2-8 µmhos/cm
pH, Reactor power > 3 MW	4.8-5.4
pH, Reactor power < 3 MW	4.8-6.0
Filterable solids (0.45 – 20 µm) before exceeding 3 MW and during operation	<0.02-0.08 ppm
Filterable solids (>20 µm)	0.025-0.05 ppm
Chloride	<0.025 ppm
Radioactivity	0.05-0.29 µCi/mL (gross/gamma based on 10 min decay after sampling)
Dissolved aluminum	1.5-4 ppb
Dissolved iron	0.5-2 ppb
Dissolved copper	0.2-1 ppb

Table 4. Coolant flow rates.

Location	Velocity	Flow Rate	Mass Flux
Outer annulus between adapter and IPT	5.1 m/s	9.93×10^{-4} m³/s	5.06×10^3 kg/m²-s
Inner annulus between basket and adapter	7.8 m/s	9.39×10^{-4} m³/s	7.23×10^3 kg/m²-s
Flow across miniplates	14.6 m/s	3.51×10^{-3} m³/s	1.44×10^4 kg/m²-s
Spacers/Confluence region	9.9 m/s	3.51×10^{-3} m³/s	9.74×10^3 kg/m²-s

Table 5. Heat transfer coefficients (W/m²-K).

Temperature (K)	Miniplates	Spacers	Inner annulus	Outer annulus
325	5.091×10^4	2.985×10^4	3.861×10^4	2.798×10^4
349	6.517×10^4	3.820×10^4	4.941×10^4	3.582×10^4
399	8.291×10^4	4.861×10^4	6.287×10^4	4.557×10^4

Stagnant water is assumed to be trapped in the small gaps where the edges of the fuel miniplates fit into the capsules and the region surrounding the rails between the outside of the capsules and the inside of the basket. A gap conductance model was used to estimate heat transfer coefficient in stagnant regions.

3.3   Neutronics Data

The results of the as-run Monte Carlo N-Particle Transport Code (MCNP) neutronic analysis performed for GTL-1 experiment during ATR Cycle 143A are documented in ECAR-1350 (Perez and Chang 2010). The MCNP input model for the GTL-1 fuel mini-plates used as-built fuel volumes, masses and densities. Heat loads were provided at four times during the cycle: BOC at 0 EFPD, MOC at 18 EFPD, MOC at 36 EFPD, and EOC at 48.9 EFPD. For the thermal analysis, the average power densities were multiplied by local to average gradients over the 8.635 × 1.829 cm fuel zone on each miniplate. The highest heat loads are located along the longitudinal edges of the fuel, therefore the finite-element mesh was refined there. Neutron flux in the ATR varies by position in the reactor and along the vertical length of the test position. Over the active core length, the heat flux magnitude varies with axial position relative to the core midplane where heat flux is highest.

3.4   Hydroxide Layer Measurements

After the experiment was removed from the reactor, post-irradiation measurements of hydroxide thickness on the miniplates were made in the hot cell at the INL Materials and Fuels Complex (Robinson

2008). Hydroxide thickness was measured using a handheld eddy current probe manufactured by Helmut Fischer DeltaScope MP30 modified for hot cell use. Instrument uncertainty is ±0.5 μm when the substrate is flat, the hydroxide layer uniform, and the probe perpendicular to the miniplate surface. Hydroxide thickness was measured in nine locations on both the front and back of each miniplate for a total of 18 measurements per miniplate. The measurement locations are shown in Figure 5 where Plane B is along the longitudinal centerline and Planes A and C are 0.635 cm from the centerline. Plane A is located near the edge that was farthest from the core. Planes 1, 2, and 3 are 3.175 cm, 5.24 cm, and 7.305 cm from the top of the miniplate, respectively. Values of hydroxide thicknesses at these measurement locations are tabulated in Table 6, along with a calculated average hydroxide thickness for each miniplate. The hydroxide layer on each miniplate is modeled as having a uniform thickness, given by the average value, which differs from miniplate to miniplate.

Figure 5. Miniplate dimensions with hydroxide measurement locations.

The miniplates near the core midplane exhibit the thickest hydroxide layers. The average of the measured hydroxide thickness values is the largest for Miniplates B3, B4, C1, C2, C3, and C4. The hydroxide thickness is somewhat uneven over the surface of the miniplates, with the minimum to maximum thickness varying by a factor of 2.5 to 4.5 for these six miniplates. Surface roughness on the cladding and the presence of the hydroxide layer growing around surface connected precipitates in the aluminum cladding can affect the eddy current measurements. A typical cladding surface finish prior to irradiation is 1.6 μm (Guillen and Yoder 2003).The peak hydroxide thickness measured is 33 μm at a point at the intersection of Plane 2 and Plane C on the back side of Miniplate C2, located in one of the highest power positions in the experiment. The average miniplate hydroxide thickness varies from a minimum of 1.7 μm on Miniplate A2 to a maximum of 21.3 μm on Miniplate C3. The average hydroxide thickness for all of the miniplates in the experiment is 12.8 μm. The thickest hydroxide measurement typically occurs along Plane 2. The standard deviation of the hydroxide measurements is larger for the miniplates closest to the core midplane, since there is more variability in the data from the mean value for those miniplates. Photographs of the front and back of Miniplate C2 taken during the visual examination of the GTL-1 miniplates are shown in Figure 6 (Robinson 2008). The contrast between lighter and darker tones along the surface of the miniplate is probably due to variations in the hydroxide composition and/or texture. Such discoloration in the heated zone is not seen on ATR driver fuel plates (Shaber 2009). The hydroxide layers showed no evidence of spalling. Miniplates fabricated with three different fuel variations (without fines, annealed, and with standard powder) performed equally well. PIE showed that irradiation-induced swelling was negligible and the fuel exhibited a normal fission density gradient (Robinson 2008).

Table 6. Measured hydroxide layer thickness (µm) (Robinson 2008).

Capsule	Miniplate	Variation	Plane	Front-A	Front-B	Front-C	Back-A	Back-B	Back-C	Average & Std. Dev.
A	A1	Std. prefilm Std. powder	1	0.4	2.3	1.7	2.4	1.6	2.9	3.1 ± 1.368
			2	1.5	3.6	5.3	3.5	4.0	5.0	
			3	1.8	3.8	4.0	4.7	3.5	4.2	
	A2	Mod. Prefilm Std. powder	1	1.3	2.6	2.5	0.9	2.1	1.9	1.7 ± 0.950
			2	1.7	3.4	2.8	1.4	1.6	3.2	
			3	1.5	0.6	0.9	0.1	0.6	0.8	
	A3	Std. prefilm Std. powder	1	8.8	8.2	12.3	5.2	8.7	7.1	10.4 ± 2.636
			2	10.1	14.1	15.9	9.5	12.4	12.8	
			3	9.1	10.3	9.5	9.5	10.4	13.3	
	A4	Std. prefilm Std. powder	1	3.2	5.0	7.5	3.2	3.1	5.1	6.8 ± 2.580
			2	8.7	8.1	12.0	8.0	7.7	10.3	
			3	5.6	5.4	7.4	5.0	6.4	10.4	
B	B1	Std. prefilm Std. powder	1	3.7	6.4	6.8	7.0	8.1	17.0	11.7 ± 5.882
			2	13.4	15.2	22.3	13.1	14.0	21.5	
			3	12.6	12.2	19.7	4.2	5.8	7.0	
	B2	Std. prefilm No fines powder	1	2.8	3.5	4.1	6.7	8.4	10.8	10.3 ± 4.769
			2	9.6	12.3	17.1	11.0	13.7	20.0	
			3	10.1	12.5	15.7	8.2	5.4	13.4	
	B3	Std. prefilm Std. powder	1	19.0	24.1	24.6	21.0	17.5	24.9	21.2 ± 7.007
			2	23.5	29.2	30.8	27.8	30.0	28.1	
			3	16.0	16.2	19.1	6.9	13.5	9.7	
	B4	Std. prefilm Annealed powder	1	17.6	14.1	14.1	15.9	15.0	21.0	19.9 ± 5.712
			2	24.9	27.9	27.9	24.0	24.8	31.0	
			3	11.1	19.8	19.8	15.3	15.3	17.9	
C	C1	Std. prefilm Std. powder	1	16.0	21.0	22.6	10.3	11.3	8.1	20.0 ± 6.378
			2	24.2	27.8	32.9	21.6	24.3	27.2	
			3	18.6	15.5	19.2	17.3	18.7	22.6	
	C2	Mod. Prefilm Std. powder	1	13.2	14.6	17.8	13.9	16.8	20.7	19.5 ± 5.822
			2	20.6	23.4	28.0	24.2	26.8	33.0	
			3	13.5	15.3	16.8	13.2	16.5	23.2	
	C3	Std. prefilm	1	18.9	17.4	12.1	12.8	14.1	14.3	21.3 ± 6.533

| Capsule	Miniplate	Variation	Plane	Front-A	Front-B	Front-C	Back-A	Back-B	Back-C	Average & Std. Dev.
		Std. powder	2	30.0	29.5	28.4	29.7	29.0	29.6	
			3	17.4	18.3	20.7	17.0	24.2	19.5	
	C4	Std. prefilm Std. powder	1	10.1	10.7	9.8	20.7	16.4	20.8	20.8 ± 6.539
			2	27.2	25.3	26.4	27.6	32.7	27.0	
			3	23.2	21.0	22.2	17.2	20.3	15.3	
D	**D1**	Std. prefilm Std. powder	1	9.4	9.6	7.5	9.5	7.9	6.3	13.7 ± 5.023
			2	23.5	19.7	18.8	20.1	17.9	17.4	
			3	15.6	15.5	13.2	12.3	11.4	11.6	
	D2	Std. prefilm No fines powder	1	11.0	8.4	10.9	8.6	13.1	14.5	9.5 ± 4.475
			2	11.4	12.0	15.7	13.2	13.0	15.6	
			3	4.4	5.7	3.4	3.0	3.1	4.6	
	D3	Std. prefilm Std. powder	1	5.0	5.9	5.0	8.9	6.2	8.4	7.8 ± 2.016
			2	11.6	9.7	10.5	9.9	8.9	9.4	
			3	8.0	7.9	7.8	6.4	6.1	5.1	
	D4	Mod. Prefilm Std. powder	1	8.1	4.9	5.4	8.9	8.3	6.3	7.9 ± 2.702
			2	10.3	10.5	10.1	14.2	10.8	9.4	
			3	6.6	7.1	6.3	3.0	6.1	5.6	
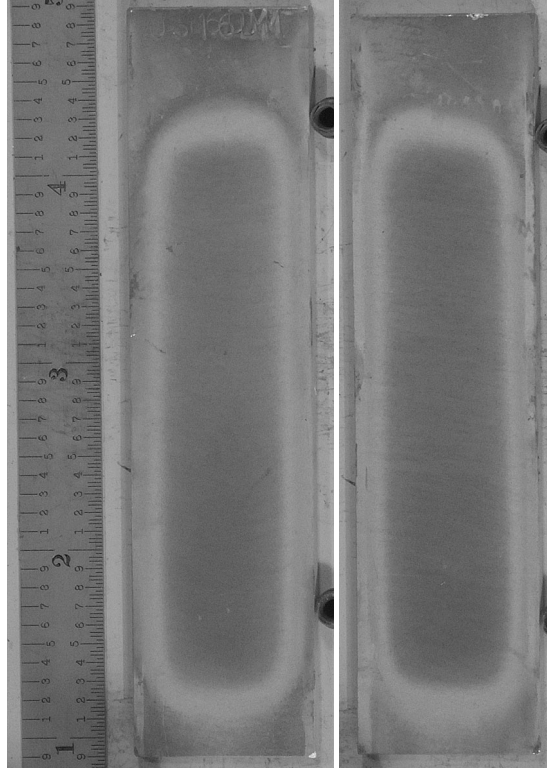
Figure 6. PIE photograph of front and back surface of miniplate C2 (Robinson 2008).

4.   RESULTS AND DISCUSSION

Figure 7 shows the predicted hydroxide temperature distribution for miniplate C2 at BOC. The contour plots show that the hottest regions of the miniplates are in the fueled zone, whereas relatively cooler temperatures are found in the aluminum border surrounding the fuel.

Figure 8 shows the variation of average hydroxide thickness as a function of calculated peak hydroxide temperature at BOC. The average hydroxide thickness increases monotonically with hydroxide temperature to a maximum value of 21.3 μm at a temperature of 194°C. This increase in measured hydroxide layer thickness at higher temperatures could be due to irregularities in surface texture and is an area where further PIE is needed. The data for the 16 miniplates appear to be clustered into three groupings at low, mid and high hydroxide temperature. The data for the six hottest miniplates are clustered at the upper right of this figure.

Figure 9 shows the predicted coolant temperature for the water channels in contact with the miniplates. In this figure, the coolant enters from the top right and flows downward towards the left. The coolant in the center coolant channel heats up more than that in the outer channels. The water heats up from an inlet temperature of 52°C to a maximum of 73°C at the outlet of Capsule D.

Results of the thermal analysis are given in a graphical (Figures 10 to 13) and tabulated (Tables 5 through 8) format at four times during the cycle: BOC at 0 EFPD, MOC at 18 EFPD, MOC at 36 EFPD, and EOC at 48.9 EFPD. The highest temperatures and heat fluxes occur at the BOC and decrease in a linear manner throughout the cycle as shown in Figure 14.

For each of the four times during the cycle, predicted peak heat flux and temperatures are given for all 16 miniplates. The "peak" value listed is the highest reported value of all nodes on the miniplate. Figures 10 to 13 show the relative magnitudes of peak fuel, cladding, hydroxide, and hydroxide-water interface temperature.

Tables 7 through 10 reveal that the predicted fuel centerline temperatures are well below the steady-state operating temperature limit of 450°C for all miniplates (Hayes 2006). The maximum hydroxide temperature is 194°C. The hydroxide layer is the thickest on miniplates B3, B4, C1, C2, C3, and C4. There is a sharp increase in hydroxide layer thickness for these plates, as compared to the other plates in the experiment. The hydroxide layer thickness averages 20.4 μm for the six hottest miniplates. The predicted peak hydroxide temperature on these six miniplates exceeds the prefilm application temperature of 185°C. These miniplates are located close to the core midplane and consequently exhibit the highest peak hydroxide heat flux and peak centerline fuel and hydroxide layer temperatures. Figure 15 shows the variation of miniplate hydroxide heat flux with axial position. The high heating near the core midplane is due to the cosine-shaped axial power profile in the reactor. The coolant heats up as it travels downwards through the test train and is less effective at removing heat from the miniplates. Calculated peak hydroxide heat flux levels for these six hottest miniplates range from 565 to 593 W/cm^2 and calculated peak steady-state fuel centerline temperatures range from 302 to 308°C. The six miniplates with the thickest hydroxide layer have the following thermal characteristics at BOC:

- Peak fuel centerline temperature ranges from 302 to 308°C
- Peak cladding temperature ranges from 218 to 221°C
- Peak hydroxide temperature ranges from 193 to 196°C
- Peak hydroxide-water interface temperature ranges from 141 to 142°C
- Peak heat flux ranges from 565 to 593 W/cm^2.

The peak hydroxide temperature occurs at the metal-oxide interface, where the hydroxide layer is in direct contact with the cladding. The peak hydroxide-water interface temperature given in Tables 7 through 10 is the temperature at the hydroxide surface in contact with the coolant water. At the hottest location on miniplate C2, there is a 51°C temperature gradient across the hydroxide layer. Due to lack of data on actual hydroxide layer growth kinetics, these results conservatively assume that the hydroxide layer thickness on the miniplates at the four time steps was that measured after irradiation. The computational results indicate that fuel centerline temperature increases by approximately 2.25°C per μm of hydroxide thickness.
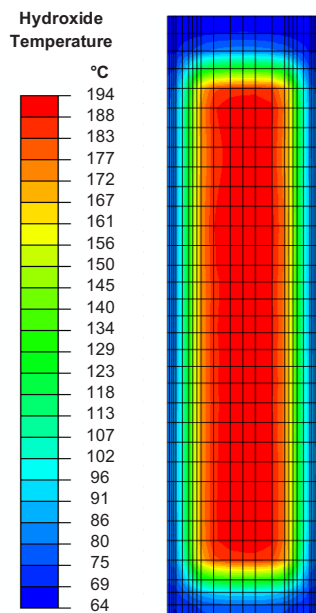
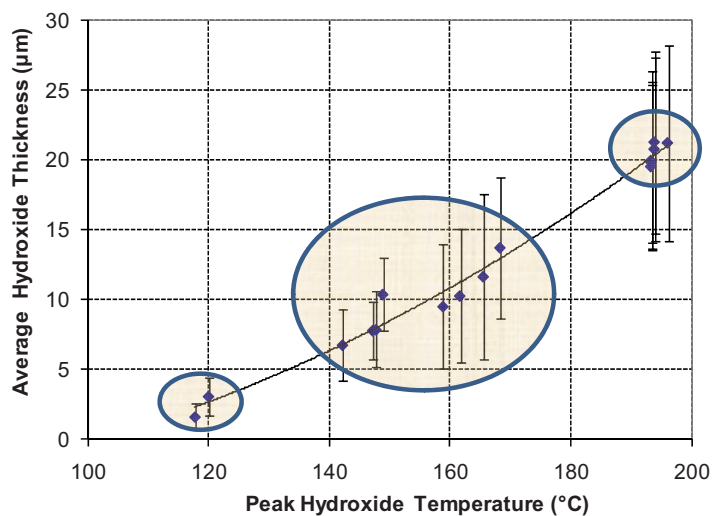**Figure 7. Predicted hydroxide temperature distribution for miniplate C2 at BOC.**

Figure 8. Average miniplate hydroxide thickness as a function of BOC peak hydroxide temperature.
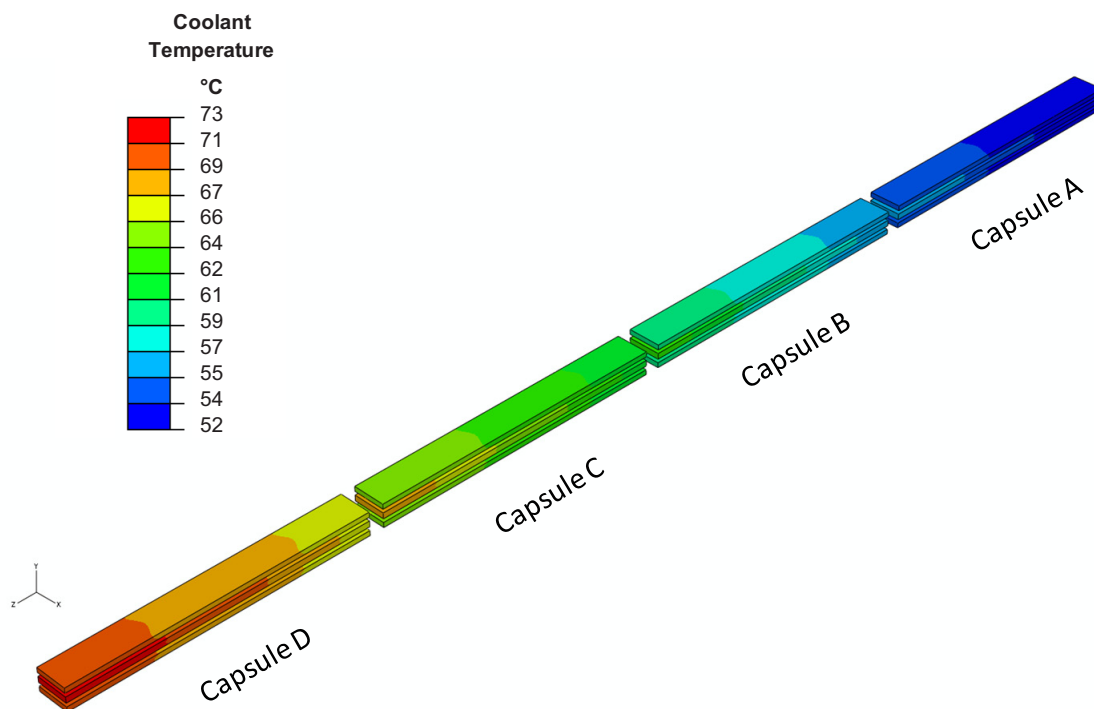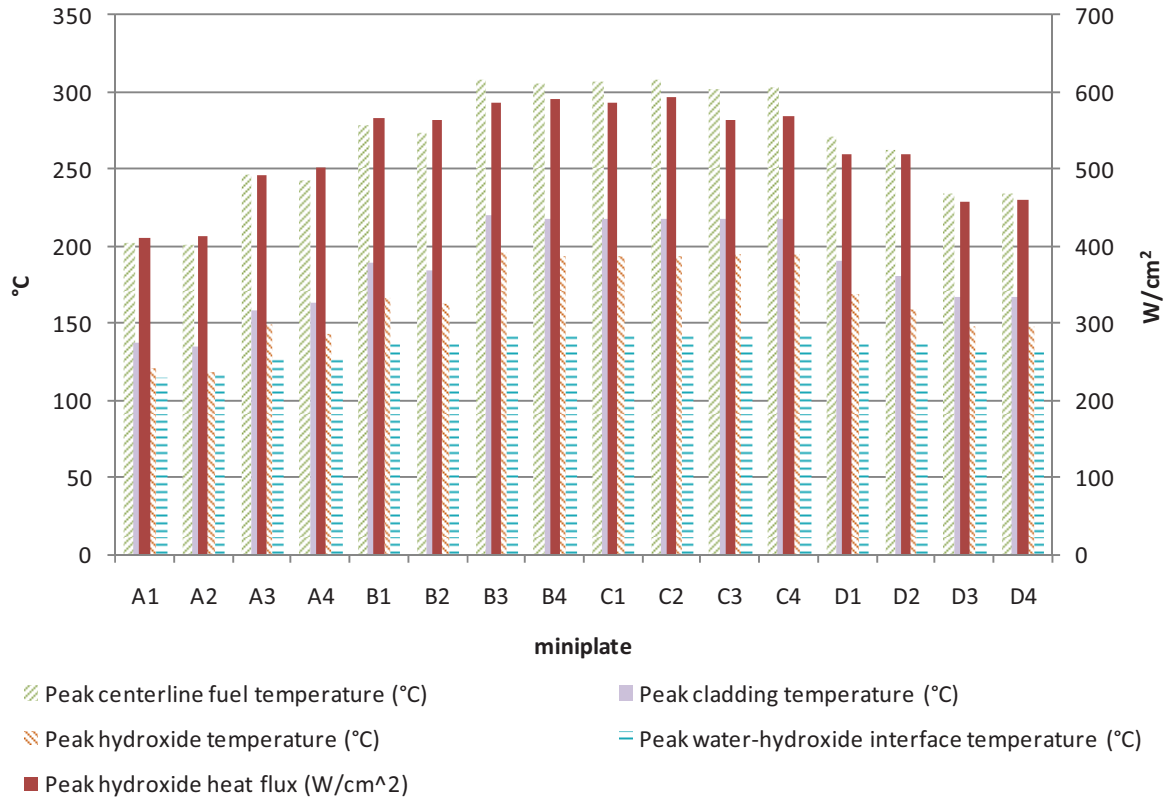

Figure 9. Water coolant temperature at BOC.

15

Figure 10. Predicted thermal behavior at BOC (0 EFPD).

Table 7. Summary of thermal predictions for BOC (0 EFPD).

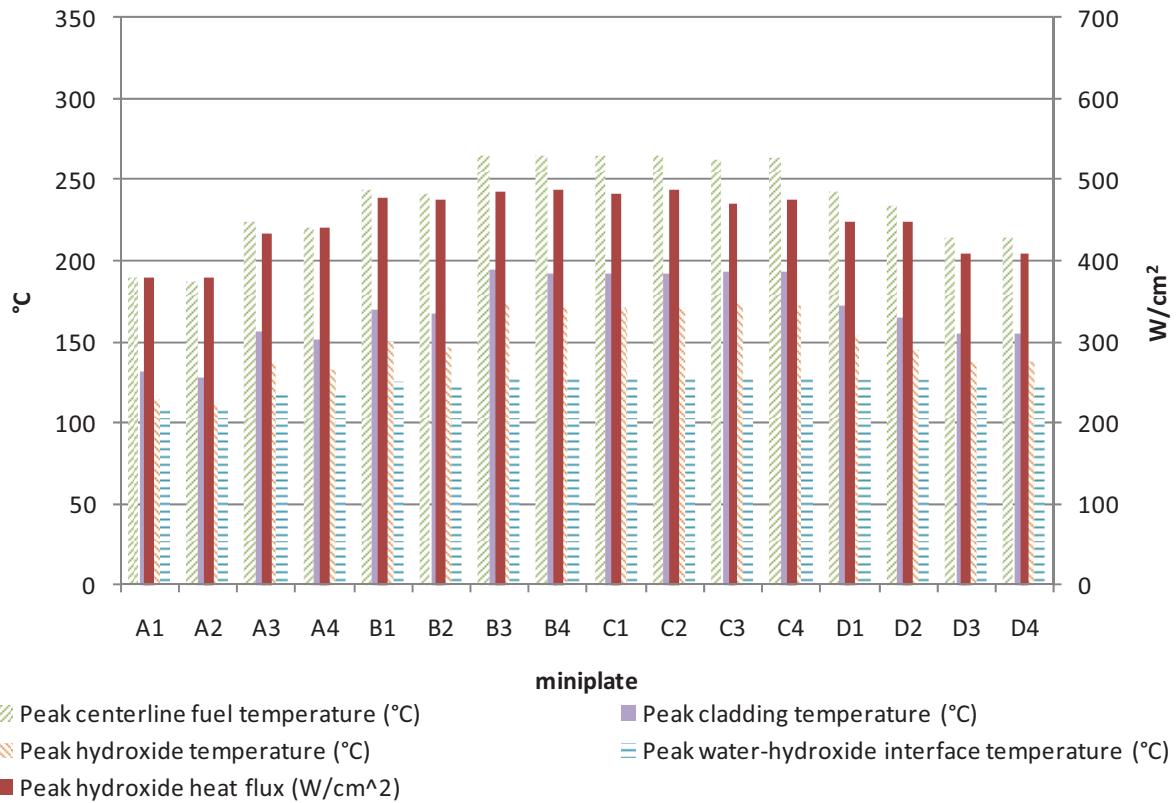| Plate	Peak Hydroxide Heat Flux	Peak Centerline Fuel Temperature	Peak Cladding Temperature	Peak Hydroxide Temperature	Peak Water-Hydroxide Interface Temperature
	W/cm^2	°C	°C	°C	°C
A1	411	202	137	120	114
A2	414	200	135	118	118
A3	493	247	159	149	126
A4	502	242	163	142	127
B1	567	278	189	166	137
B2	564	274	185	162	136
B3	587	308	221	196	141
B4	590	306	218	193	141
C1	587	307	218	193	142
C2	593	308	218	194	142
C3	565	302	218	194	141
C4	570	303	218	194	142
D1	520	271	191	168	137
D2	520	262	181	159	137
D3	457	233	167	147	132
D4	459	234	167	148	132

16

Figure 11. Predicted thermal behavior at MOC (18 EFPD).

Table 8. Summary of thermal predictions for MOC (18 EFPD).

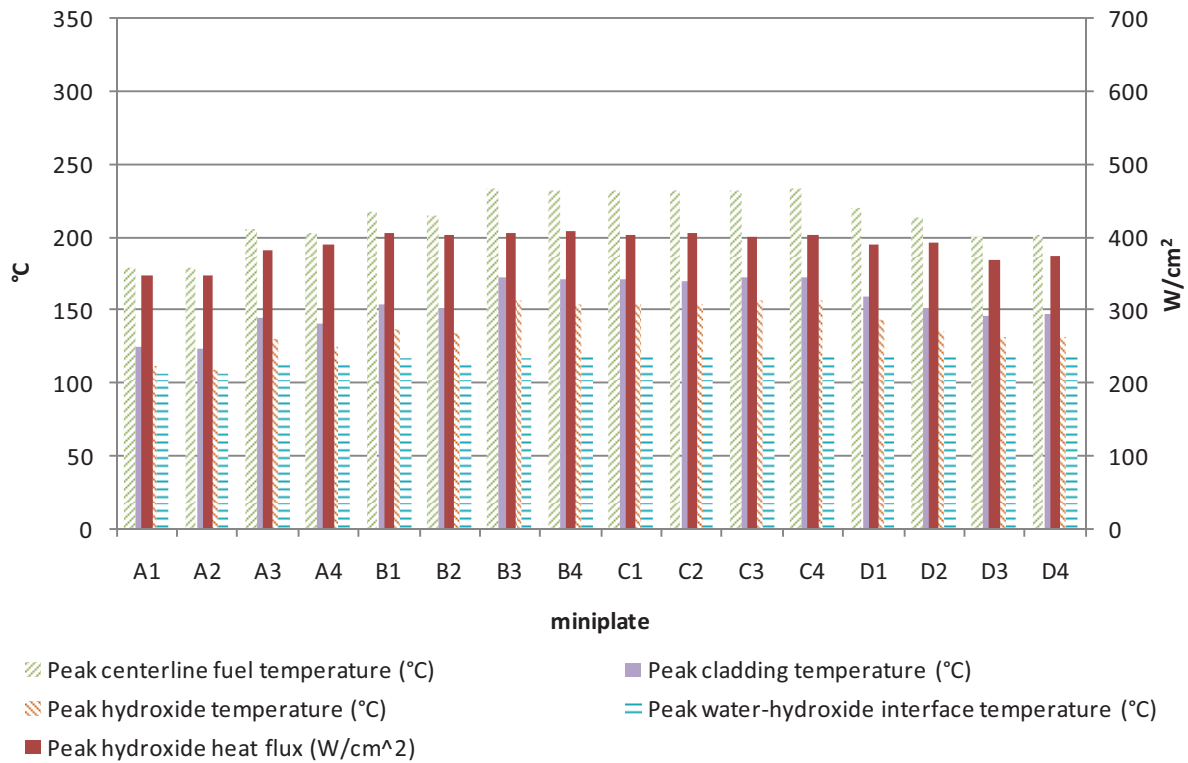| Plate	Peak Hydroxide Heat Flux	Peak Centerline Fuel Temperature	Peak Cladding Temperature	Peak Hydroxide Temperature	Peak Water-Hydroxide Interface Temperature
	W/cm²	°C	°C	°C	°C
A1	378	190	131	115	110
A2	378	187	128	113	110
A3	432	224	156	138	118
A4	441	221	151	133	119
B1	477	244	170	150	126
B2	475	241	167	147	125
B3	485	266	194	173	128
B4	488	264	192	171	128
C1	483	264	192	171	128
C2	487	265	192	171	129
C3	470	263	193	173	129
C4	476	263	193	173	129
D1	447	242	173	154	127
D2	447	234	164	146	127
D3	408	214	155	138	124
D4	409	215	156	138	124

17

Figure 12. Predicted thermal behavior at MOC (36 EFPD).

Table 9. Summary of thermal predictions for MOC (36 EFPD).

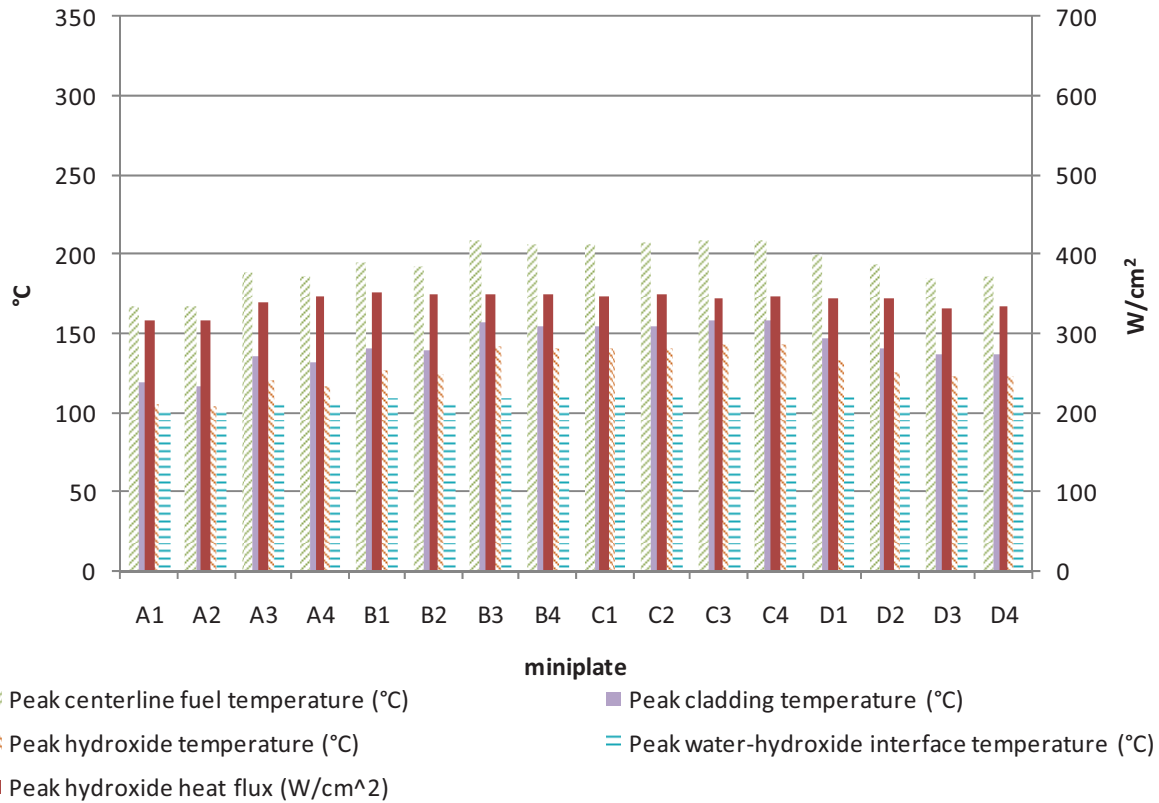| Plate	Peak Hydroxide Heat Flux	Peak Centerline Fuel Temperature	Peak Cladding Temperature	Peak Hydroxide Temperature	Peak Water-Hydroxide Interface Temperature
	W/cm²	°C	°C	°C	°C
A1	346	179	125	111	106
A2	348	178	123	108	106
A3	382	205	145	129	112
A4	390	202	141	124	113
B1	404	216	153	137	116
B2	402	213	151	134	116
B3	405	232	172	156	117
B4	407	231	171	153	118
C1	404	231	171	153	118
C2	406	231	170	153	118
C3	399	232	173	156	119
C4	402	232	173	156	119
D1	391	219	159	142	118
D2	392	213	152	135	119
D3	370	199	146	131	117
D4	373	201	147	131	118

18

Figure 13. Predicted thermal behavior at EOC (48.9 EFPD).

Table 10. Summary of thermal predictions for EOC (48.9 EFPD).

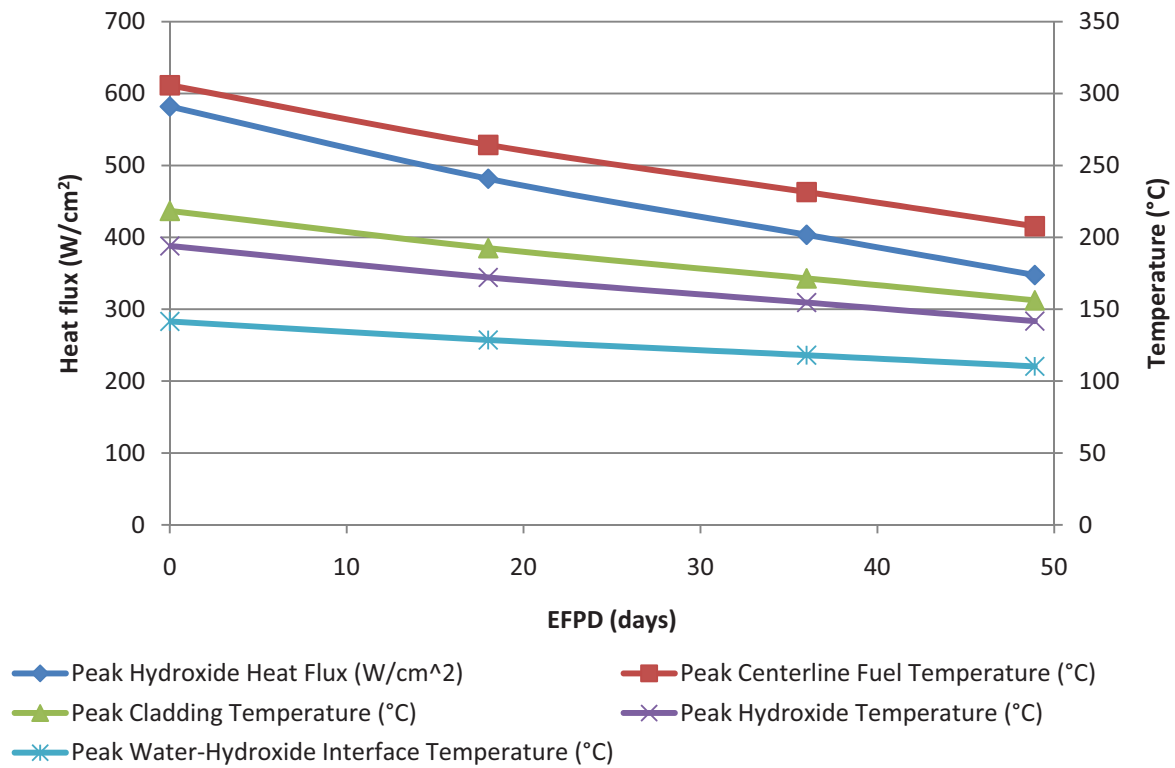| Plate	Peak Hydroxide Heat Flux	Peak Centerline Fuel Temperature	Peak Cladding Temperature	Peak Hydroxide Temperature	Peak Water-Hydroxide Interface Temperature
	W/cm^2	°C	°C	°C	°C
A1	316	168	119	106	102
A2	317	167	117	104	102
A3	338	188	136	121	106
A4	346	186	132	117	107
B1	351	196	141	127	109
B2	349	193	139	124	108
B3	348	208	157	142	109
B4	350	207	155	141	110
C1	346	207	155	141	110
C2	349	207	155	141	110
C3	345	208	158	143	111
C4	347	209	158	143	111
D1	344	200	147	133	112
D2	344	194	141	126	112
D3	331	184	137	123	112
D4	334	186	137	123	112

Figure 14. Variation with irradiation time of heat flux and peak temperatures for the six hottest miniplates.
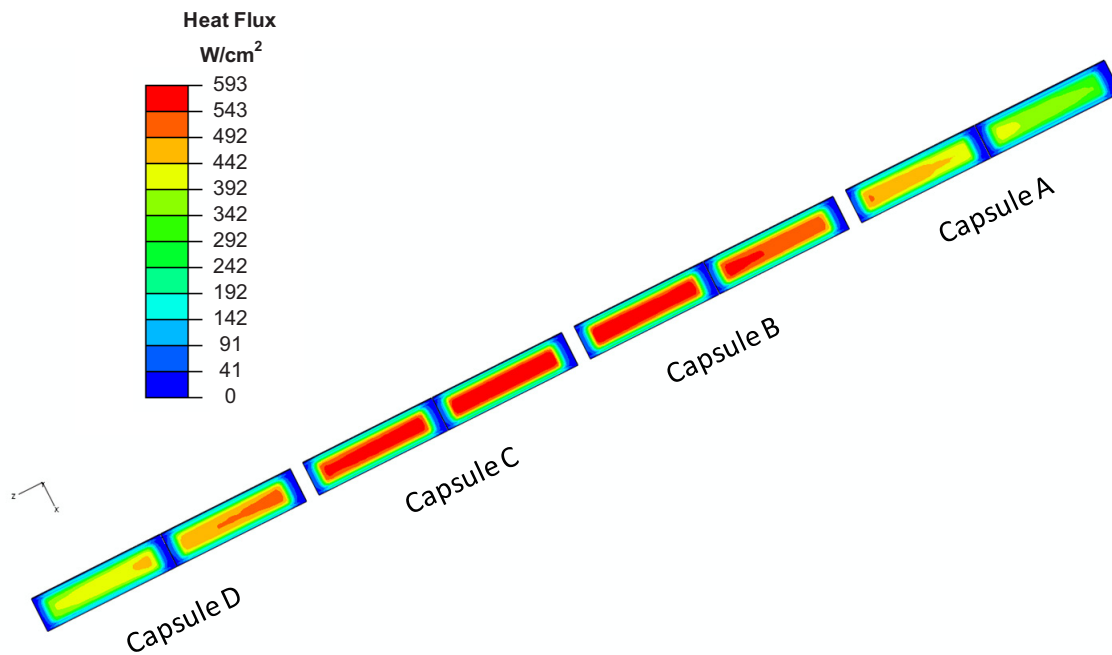

Figure 15. Variation of miniplate hydroxide heat flux with axial position.

5. SUMMARY

The GTL-1 experiment was conducted to assess corrosion the performance of the proposed BFFL booster fuel at heat flux levels ~30% above the design operating condition. Sixteen miniplates fabricated from 25% enriched, high-density U_3Si_2/Al dispersion fuel with 6061 aluminum cladding were subjected to peak BOC heat fluxes ranging from 411 W/cm^2 to 593 W/cm^2. Miniplates fabricated with three different fuel variations (without fines, annealed, and with standard powder) exhibited negligible irradiation-induced swelling and a normal fission density gradient (Robinson 2008). Both the standard and the modified prefilm procedures produced hydroxide films that adequately protected the miniplates from excessive corrosion.

A detailed finite element model was constructed to calculate temperatures and heat flux for an as-run cycle average effective south lobe power of 25.4 MW(t). Results of the thermal analysis are given at four times during the cycle: BOC at 0 EFPD, MOC at 18 EFPD, MOC at 36 EFPD, and EOC at 48.9 EFPD. The highest temperatures and heat fluxes occur at the BOC and decrease in a linear manner throughout the cycle.

Miniplate heat flux levels and fuel, cladding, hydroxide, and coolant-hydroxide interface temperatures were calculated using the average measured hydroxide thickness on each miniplate. The hydroxide layers are the largest on miniplates nearest to the core midplane, where heat flux and temperature are highest. As shown in Figure 8, the hydroxide layer thickness increases monotonically with peak hydroxide temperature. The hydroxide layer exhibits a marked increase in thickness for the hottest plates. The reported thicknesses are clustered into three groupings at high, mid and low hydroxide temperatures. The six hottest miniplates (B3, B4, C1, C2, C3, and C4) have the following thermal characteristics at BOC:

- Peak fuel centerline temperature >300°C

- Peak cladding temperature >200°C

- Peak hydroxide temperature >190°C

- Peak hydroxide-water interface temperature >140°C

- Peak heat flux >565 W/cm^2.

6. RECOMMENDATIONS FOR FUTURE STUDIES

The following recommendations are provided to gain a better understanding of the miniplate surface hydroxide layer formed during irradiation.

1. *Recommendation*: Rerun the thermal analysis using ABAQUS CFD.

   Rationale: The existing thermal models for RERTR and GTL-1 are constructed using a bulk flow approach to modeling of the water channels. Modeling the flow channels using the CFD tool that became available in the 6.10 release of ABAQUS would provide details on the flow behavior through the test train. Researchers have found the properties of the boehmite layer strongly depend upon the agitation, atmosphere, and pressure of the water flow (Wang 2009). There are significant differences between hydroxide layers formed under static versus flowing conditions. This analysis may shed light on the differences in measured hydroxide thickness between the GTL-1 and the RERTR miniplates (Robinson and Finlay 2007). The GTL-1 design holds two plates per level, whereas the RERTR design holds four plates per level. The flow channels adjacent to the miniplates are more than 50% larger for the GTL-1 test train than for the RERTR test train. The RERTR-12 design relies upon a total of five coolant channels—three inner flow channels that are 0.234 cm wide and two outer flow channels that are 0.146 cm wide—to provide cooling to the miniplates (Roth 2009). In comparison, the GTL-1 design has three water coolant channels that are 0.36 cm wide adjacent to the miniplates.

2. *Recommendation*: Perform in-depth PIE of the hydroxide layer formed on the miniplates.

   Rationale: Thicker hydroxide layers were observed on the GTL-1 miniplates wherein the peak hydroxide temperature exceeded the prefilm application temperature of 185°C. Further PIE is recommended to investigate possible microstructural changes in the hydroxide layers on these miniplates. Further PIE of the hydroxide phase and composition should be conducted, including microstructural analysis and x-ray diffraction to determine phase composition, crystal size, morphology, and porosity. The presence of precipitates protruding from the surface can dramatically increase the surface texture of the cladding and skew the eddy current measurements. Relative roughness of the discolored areas of the miniplates should be examined and an analysis should be performed to quantify concentrations of Fe, Cu, Si, Mg, and Mn. The effect of microstructure on the thermophysical properties and stability of the hydroxide layer should be quantified. The thermal conductivity of hydroxide films formed during irradiation in the reactor may be significantly lower than ex-reactor formed films (Polkinghorne and Lacy 1991). A film with a lower thermal conductivity reduces heat transfer from the fuel to the coolant, thus leading to higher plate temperatures. Additional work in this area would aid in establishing a safe maximum hydroxide operating temperature to prevent excessive growth that could lead to fuel plate failure.

3. *Recommendation*: Conduct a well-controlled, fundamental study on irradiated hydroxide layer to elucidate the mechanisms of hydroxide layer growth.

   Rationale: It is well established in literature that the corrosion conditions in the reactor differ significantly from those in the autoclave (Wintergerst 2009). The corrosion product that forms on the surface of the fuel cladding during irradiation is typically much thicker than that obtained in the autoclave. Thermal hydraulic conditions (e.g., coolant velocity, turbulence, temperature), surface radiolysis, and water chemistry are factors that can contribute to these differences. The presence of crud (nonfilterable solids from the reactor coolant), contaminants or precipitates can drastically alter the boehmite surface texture and composition. Degradation of the electropositive passivation of the hydroxide layer surrounding the surface precipitate particles should be examined. A well-controlled study is needed to develop a fundamental understanding of how the hydroxide grows and changes during reactor operation.

4. *Recommendation*: Effects caused by the chemical reaction between fuel and matrix materials should be evaluated.

Rationale: Prior experiments of U_3Si_2/Al fuel irradiated at the High Flux Isotope Reactor showed that the aluminum-U_3Si_2 interdiffusion process results in the formation of the intermetallic compound $U(AlSi)_3$ in the diffusion zone at the U_3Si_2/Al interface. Hofman et al. (1996) observed that these interaction zones grow in extent as operating temperature and fission rates are increased. The BFFL Final Report (INL 2009) includes PIE images that reveal aluminum silicide zones around the fuel particles. Some fuel particles appear to be U_3Si rather than U_3Si_2, which can be attributed to the aluminum-silicon reaction depleting silicon from the uranium silicide. Thermal effects from the heat of reaction (approximately 350 J/g of U_3Si_2 reacted) (NUREG-1313 1988) are 26.5 J/cm^2 for each miniplate, producing a very small heat release for the large reaction times associated with diffusion (Hofman et al. 1996). The calculations presented in this report do not include radiation-induced changes to the thermophysical properties. As the irradiation cycle progressed, the thermophysical properties of the fuel employed by the ABAQUS model were not varied to reflect changes in the fuel (burnup, interdiffusion, etc.) because no such data was available.

7.   REFERENCES

Beckwith, R., 2011, ATR coolant chemistry history, personal communication.

Bourns, W. T., 1968, "*Corrosion Testing of Uranium Silicide Fuel Specimens*," AECL-2718, Atomic Energy of Canada Limited, September 1968.

Byalobzheskii, A. V., 1963, "*The Effect of Neutron Irradiation on the Corrosion of Aluminum in Water*," Institute of Physical Chemistry, Academy of Sciences, USSR, May 1963.

Dassault Systèmes Simulia Corp., 2007, *ABAQUS/Standard*, Version 6.7-3 (2007).

Guillen, D. P., 2008, "Thermal Analysis of Gas Test Loop-1 (GTL-1) Miniplate Irradiation Experiment," ECAR-62, Idaho National Laboratory.

Guillen, D. P., and Murray, P., 2009, "Thermal Analysis of Gas Test Loop-1 (GTL-1) Miniplate Irradiation Experiment," Idaho National Laboratory, *Proceedings of the 13th Nuclear Thermal Hydraulics Meeting (Nureth-13)*, September 28–October 1, 2009, Kanazawa, Japan.

Guillen, D. P., and Yoder, T. S., 2008, "Thermal Hydraulic Effects of Fuel Plate Surface Roughness," *Nuclear Engineering and Design*, Vol. 238, pp. 2480-2483.

Hayes, S. L., 2006, "High Temperature Performance of Silicide Dispersion Fuels," EDF-7450, Idaho National Laboratory.

Hayes, S. L., 2008, "U_3Si_2/Al Miniplate Irradiation Test Plan to Support the BFFL Booster Fuel Concept," PLN-2735, Idaho National Laboratory, February 2008.

Hofman, G. L., et al., 1996, "Aluminum-U_3Si_2 Interdiffusion and its Implications for the Performance of Highly Loaded Fuel Operating at Higher Temperatures and Fission Rates," in *Proc. of the 19th International Meeting on Reduced Enrichment for Research and Test Reactors*, Seoul, Korea, October 1996.

Incropera, F. P. and DeWitt, D. P., 2002, *Fundamentals of Heat and Mass Transfer*, 5th ed., John Wiley & Sons, New York, 2002.

INL, 2009, "*Boosted Fast Flux Loop Final Report*," Idaho National Laboratory External Report, INL/EXT-09-16413, Idaho National Laboratory, July 2009.

Leenaers, A., et al., 2004, "Microstructure of U_3Si_2 Fuel Plates Submitted to a High Heat Flux," *Journal of Nuclear Materials*, Vol. 327, pp. 121–129.

Longhurst, G. R., and Khericha, S. T., 2005, "*Boosted Fast Flux Loop Technical and Functional Requirements*," Draft, Rev. A, INL/EXT-04-02273, Idaho National Laboratory, July 2005.

Murray, P. E., 2008, "Validation of ABAQUS Standard 6.7-3 Heat Transfer," ECAR-131, Idaho National Laboratory, January 30, 2008.

Perez, D. M., and Chang, G. S., 2010, "As-Run Neutronics Analysis of the GTL-1 Experiment Irradiated in ATR South Flux Trap," ECAR-1245, Idaho National Laboratory.

Perry, R. H., and Green, D. W., 1997, *Perry's Chemical Engineers' Handbook*, 7th Edition, McGraw-Hill, 1997.

Polkinghorne, S. T., and Lacy, J. M., 1991, *Thermophysical and Mechanical Properties of ATR Core Materials*, Idaho National Laboratory, August 1991.

Robinson, A. B., 2008, "GTL Non-Destructive Examination Results," ECAR-677, Idaho National Laboratory, July 24, 2008.

Robinson, A. G., and Finlay, M. R., 2007, "*RERTR-7 Post Irradiation Examination (PIE) Letter Report*," INL/EXT-07-13271, Idaho National Laboratory, September 2007.

Roth, G. A., 2008, "RERTR-12 Thermal and Hydraulic Analysis Report," ECAR-768, Idaho National Laboratory, September 29, 2008.

Shaber, E., 2009, email communication, December 22, 2009.

Shaber, E., and Hofman, G., 2005, "*Corrosion Minimization for Research Reactor Fuel*," Idaho National Laboratory, INL/EXT-05-00256, Idaho National Laboratory, June 2005.

NUREG-1313, 1988, "Safety Evaluation Report Related to the Evaluation of Low-Enriched Uranium Silicide-Aluminum Dispersion Fuel for Use in Non-Power Reactors," U.S. Nuclear Regulatory Commission, July 1988.

"Upgraded Final Safety Analysis Report for the Advanced Test Reactor," Idaho National Laboratory, SAR-153, Chapter 5 – Primary Coolant System, Rev. 14, February 15, 2011.

Wachs, D. M., 2006, "GTL Miniplate Experiment Flow Test," EDF-7531, Idaho National Laboratory, November 2006.

Wang, J. Q., et al., 2009, "Hydrothermal Transformation of Bayerite to Boehmite." *Science of Advanced Materials*, Vol. 1, Issue 1, pp. 77–85.

Wintergerst, M. et al., 2009, "Corrosion of the AlFeNi Alloy used for the Fuel Cladding in the Jules Horowitz Research Reactor," *Journal of Nuclear Materials*, Vol. 393, pp. 369–380

APPENDIX

THERMOPHYSICAL PROPERTIES OF MINIPLATE MATERIALS
USED IN THE ANALYSIS

APPENDIX

Thermophysical properties for aluminum alloy 6061 (Thermophysical and Mechanical Properties of ATR Core Materials, EG&G Idaho, Inc., Report No. PG-T-91-031, August 1991):

$$T_{al6061} = \begin{pmatrix} 400 \\ 500 \\ 600 \\ 700 \\ 800 \\ 855 \end{pmatrix} \cdot K \qquad c_p = \begin{pmatrix} 942 \\ 978 \\ 1034 \\ 1080 \\ 1126 \\ 1151 \end{pmatrix} \frac{J}{kg \cdot K} \qquad c_p = \begin{pmatrix} 0.225 \\ 0.236 \\ 0.247 \\ 0.258 \\ 0.269 \\ 0.275 \end{pmatrix} \frac{BTU}{lb \cdot R}$$

$$T = \frac{T_{al6061} - 273\,K}{1 \cdot K} \qquad T = \begin{pmatrix} 127 \\ 227 \\ 327 \\ 427 \\ 527 \\ 582 \end{pmatrix} \qquad \begin{pmatrix} 127 \\ 227 \\ 327 \\ 427 \\ 527 \\ 582 \end{pmatrix} \, ^\circ C = \begin{pmatrix} 261 \\ 441 \\ 621 \\ 801 \\ 981 \\ 1080 \end{pmatrix} \, ^\circ F$$

$$\rho_{al6061} = 2702 \cdot \frac{kg}{m^3} \qquad\qquad \rho_{al6061} = 0.098 \cdot \frac{lb}{in^3}$$

$$T_{al6061} := \begin{pmatrix} 400 \\ 450 \\ 500 \\ 550 \\ 600 \\ 650 \\ 700 \\ 750 \\ 800 \\ 855 \end{pmatrix} \cdot K \qquad k_{al6061} := \begin{pmatrix} 177 \\ 179 \\ 188 \\ 191 \\ 190 \\ 188 \\ 185 \\ 182 \\ 179 \\ 175 \end{pmatrix} \cdot \frac{W}{m \cdot K} \qquad k_{al6061} = \begin{pmatrix} 0.002367 \\ 0.002394 \\ 0.002514 \\ 0.002555 \\ 0.002541 \\ 0.002514 \\ 0.002474 \\ 0.002434 \\ 0.002394 \\ 0.002341 \end{pmatrix} \cdot \frac{BTU}{s \cdot in \cdot R}$$

$$T := \frac{T_{al6061} - 273 \cdot K}{1 \cdot K} \qquad T = \begin{pmatrix} 127 \\ 177 \\ 227 \\ 277 \\ 327 \\ 377 \\ 427 \\ 477 \\ 527 \\ 582 \end{pmatrix} \qquad \begin{pmatrix} 127 \\ 177 \\ 227 \\ 277 \\ 327 \\ 377 \\ 427 \\ 477 \\ 527 \\ 582 \end{pmatrix} \cdot {}^{\circ}C = \begin{pmatrix} 261 \\ 351 \\ 441 \\ 531 \\ 621 \\ 711 \\ 801 \\ 891 \\ 981 \\ 1080 \end{pmatrix} \cdot {}^{\circ}F$$

$\varepsilon := 0.09$ at 212 °F   Emissivity from Holman, J.P., <u>Heat Transfer</u>, McGraw Hill, Ninth Edition, 2002, p. 607

Thermophysical properties for boehmite (Thermophysical and Mechanical Properties of ATR Core Materials, EG&G Idaho, Inc., Report No. PG-T-91-031, August 1991):

$$T_{boehmite} := \begin{pmatrix} 400 \\ 500 \\ 600 \\ 700 \\ 800 \\ 900 \\ 1000 \\ 1100 \\ 1200 \end{pmatrix} \cdot K \qquad c_p := \begin{pmatrix} 1349 \\ 1538 \\ 1704 \\ 1844 \\ 1959 \\ 2049 \\ 2113 \\ 2151 \\ 2164 \end{pmatrix} \cdot \frac{J}{kg \cdot K} \qquad c_p = \begin{pmatrix} 0.322 \\ 0.367 \\ 0.407 \\ 0.44 \\ 0.468 \\ 0.489 \\ 0.505 \\ 0.514 \\ 0.517 \end{pmatrix} \cdot \frac{BTU}{lb \cdot R}$$

$$\rho_{boehmite} := 3010 \cdot \frac{kg}{m^3} \qquad\qquad \rho_{boehmite} = 0.109 \cdot \frac{lb}{in^3}$$

$$k_{boehmite} := 2.25 \cdot \frac{W}{m \cdot K} \qquad\qquad k_{boehmite} = 3.009 \times 10^{-5} \cdot \frac{BTU}{s \cdot in \cdot R}$$

$\varepsilon := 0.8 \qquad$ at 673 K $\qquad$ Emissivity from Wefers, K., and Misra, C., *Oxides and Hydroxides of Aluminum*, Alcoa Laboratories, 1987, p. 18-23.

Thermophysical properties for U_3Si_2-Al dispersion fuel (Research Reactor Core Conversion Guidebook, IAEA-TECDOC-643, Vol. 4: Fuels, Appendices I-K):

$$T_u := \begin{pmatrix} 400 \\ 500 \\ 600 \\ 700 \\ 800 \\ 900 \\ 1000 \\ 1100 \\ 1200 \end{pmatrix} \cdot K \qquad T_{usi} := \frac{T_u - 273 \cdot K}{1 \cdot K} \qquad T_{usi} = \begin{pmatrix} 127 \\ 227 \\ 327 \\ 427 \\ 527 \\ 627 \\ 727 \\ 827 \\ 927 \end{pmatrix} \qquad \begin{pmatrix} 127 \\ 227 \\ 327 \\ 427 \\ 527 \\ 627 \\ 727 \\ 827 \\ 927 \end{pmatrix} {}^{\circ}C = \begin{pmatrix} 261 \\ 441 \\ 621 \\ 801 \\ 981 \\ 1161 \\ 1341 \\ 1521 \\ 1701 \end{pmatrix} \cdot {}^{\circ}F$$

$$c_{pu} := \left(0.199 + 0.000104 \cdot T_{usi}\right) \frac{J}{gm \cdot K}$$

c_p values are for U_3Si_2 and don't account for aluminum dispersion, which would increase c_p. Therefore, ABAQUS calculations are conservative.

29

$$\rho_{usi} := (6.2 \cdot 1.175) \cdot \frac{gm}{cm^3} \qquad \rho_{usi} = 0.263 \cdot \frac{lb}{in^3}$$

$$k_{usi} := 20 \cdot \frac{W}{m \cdot K} \qquad k_{usi} = 2.675 \times 10^{-4} \cdot \frac{BTU}{s \cdot in \cdot R} \qquad c_p = \begin{pmatrix} 0.051 \\ 0.053 \\ 0.056 \\ 0.058 \\ 0.061 \\ 0.063 \\ 0.066 \\ 0.068 \\ 0.071 \end{pmatrix} \frac{BTU}{lb \cdot R}$$